

WILEY-VCH



European Chemical  
Societies Publishing

# Take Advantage and Publish Open Access



By publishing your paper open access, you'll be making it immediately freely available to anyone everywhere in the world.

That's maximum access and visibility worldwide with the same rigor of peer review you would expect from any high-quality journal.

**Submit your paper today.**



[www.chemistry-europe.org](http://www.chemistry-europe.org)

# Ru-P Nanoalloy from Elemental Phosphorus as P-Source: Synthesis, Characterization and Catalytic Evaluation

Matteo Vanni,<sup>[a, b]</sup> Giacomo Provinciali,<sup>[a]</sup> Fuencisla Delgado Calvo,<sup>[a]</sup> Elisa Carignani,<sup>[b, c]</sup> Sébastien Dreyfuss,<sup>[d]</sup> Nicolas Mézailles,<sup>[d]</sup> Antonio Massimiliano Mio,<sup>[e]</sup> Giuseppe Nicotra,<sup>[e]</sup> Stefano Caporali,<sup>[f]</sup> Silvia Borsacchi,<sup>[b, c]</sup> Maurizio Peruzzini,<sup>[a]</sup> and Maria Caporali\*<sup>[a]</sup>

Binary ruthenium-phosphorus nanoparticles (NPs) with different Ru/P ratio were prepared in mild conditions using white phosphorus (P<sub>4</sub>) as phosphorus source. Accurate study of both their morphology and structure at the atomic level by TEM and HAADF-STEM, respectively, showed that Ru<sub>2</sub>P and RuP have a narrow size distribution (ca. 3.3 nm) and are lacking an ordered ruthenium phosphide lattice. <sup>31</sup>P Solid State NMR highlighted the existence of three different phosphorus species consistently

with the lack of a metal phosphide lattice and finally XPS revealed that the true nature of these nanoparticles can be better described as a ruthenium-phosphorus alloy. As a benchmark test, the selective hydrogenation of nitroarenes to primary aromatic amines was studied and evidenced how the P-alloying imparts a surface modification resulting in a higher catalytic activity and excellent chemoselectivity of Ru<sub>2</sub>P in comparison to Ru(0) and RuP.

## Introduction

Transition metal phosphides have gained an increasing attention in the last decades thanks to the discovery of their wide application in key-technologies as lithium-ion batteries, superconductivity and catalysis. Concerning the latter field, the initial studies in the 1990s addressed the use of metal phosphides

mainly in hydrotreating processes as the hydrodeoxygenation,<sup>[1]</sup> hydrodesulfurization<sup>[2,3]</sup> and hydrodenitrogenation<sup>[4]</sup> reactions, while recently the outstanding performance of nanostructured metal phosphides as electrocatalysts in water splitting has emerged.<sup>[5]</sup> In particular, ruthenium phosphides represent good candidates to replace not only ruthenium metal, which has the drawback of being poorly stable in electrolytic conditions, but also platinum-group metals in the hydrogen evolution reaction (HER), showing comparable performance while being stable at all pH values.<sup>[6–10]</sup> Moving into the field of organic synthesis, little has been explored concerning the application of metal phosphides,<sup>[11]</sup> though recently it has been shown how phosphorus-alloying can be a powerful tool for constructing highly active and robust catalysts.<sup>[12]</sup> For instance, in the reaction of reduction of nitroarenes to anilines, nanostructured transition metals<sup>[13]</sup> have assumed a leading position and as far as we know, at industrial level the process makes use exclusively of a solid heterogeneous catalyst. Although molecular complexes have been reported, none of them can compete with the solid catalyst once a large scale continuous process needs to be set. Hence the interest in developing a strategy for the synthesis of nanostructured ruthenium phosphides able to control the nanoparticles dimension and to fine tuning the stoichiometry of the phosphides which has correspondingly a key role in the catalytic activity.

The preparation of ruthenium phosphide nanoparticles has been so far accomplished by H<sub>2</sub>-thermal treatment, which requires drastic reaction conditions. Temperatures above 550 °C are indeed necessary for the reduction of the ruthenium salt, and a large excess of either phosphate<sup>[14]</sup> or hypophosphite salt<sup>[15]</sup> is necessary as “P” source. A drawback of this method is the need of post-treatment of the produced ruthenium phosphide to remove the saline impurities formed during the thermal decomposition. Zhang and co-workers have shown that ruthenium phosphides may be produced also by H<sub>2</sub>-thermal treatment using triphenylphosphine as phosphorus

[a] M. Vanni, G. Provinciali, F. D. Calvo, M. Peruzzini, Dr. M. Caporali  
Istituto di Chimica dei Composti Organometallici  
Consiglio Nazionale delle Ricerche  
Via Madonna del Piano 10  
50019 Sesto Fiorentino (Italy)  
E-mail: maria.caporali@iccom.cnr.it


[b] M. Vanni, E. Carignani, S. Borsacchi  
Istituto di Chimica dei Composti Organometallici  
Consiglio Nazionale delle Ricerche  
Via G. Moruzzi 1  
56124 Pisa (Italy)


[c] E. Carignani, S. Borsacchi  
Center for Instrument Sharing of the University of Pisa (CISUP)  
Largo Bruno Pontecorvo 3  
56127 Pisa (Italy)

[d] S. Dreyfuss, N. Mézailles  
Laboratoire Hétérochimie Fondamentale et Appliquée  
UMR 5069 CNRS,  
Université Paul Sabatier  
118, Route de Narbonne  
31062 Toulouse (France)

[e] A. M. Mio, G. Nicotra  
CNR-IMM Istituto per la Microelettronica e Microsistemi  
VIII strada 5  
I-95121 Catania (Italy)

[f] S. Caporali  
Department of Industrial Engineering  
University of Florence  
Via di S. Marta 3  
50139 Florence (Italy)

 Supporting information for this article is available on the WWW under <https://doi.org/10.1002/cctc.202200685>

 © 2022 The Authors. ChemCatChem published by Wiley-VCH GmbH. This is an open access article under the terms of the Creative Commons Attribution License, which permits use, distribution and reproduction in any medium, provided the original work is properly cited.

source.<sup>[16]</sup> Recently, triphenylphosphite was also proved to be a suitable phosphatizing agent, with the advantage of not requiring too harsh conditions (heating up to only 300 °C).<sup>[17]</sup> In 2008, some of us<sup>[18]</sup> developed a novel method to synthesize nickel phosphide nanoparticles (Ni<sub>2</sub>P) using white phosphorus as 'P'-source. The method encompasses the reaction of stoichiometric amount of elemental phosphorus with nickel complexes, such as Ni(acac)<sub>2</sub> or Ni(cod)<sub>2</sub> (acac = acetylacetonate, cod = cyclo-octa-1,5-diene), or with preformed Ni(0) nanoparticles. Since then, the synthesis of a wide-ranging variety of metal phosphide nanoparticles, such as FeP, Cu<sub>3</sub>P, Pd<sub>5</sub>P<sub>2</sub>,<sup>[19]</sup> InP, Zn<sub>3</sub>P<sub>2</sub>,<sup>[20]</sup> and Au<sub>2</sub>P<sub>3</sub><sup>[21]</sup> has been carried out smoothly in solution using white phosphorus. In the present work, our aim has been the synthesis of Ru–P nanoparticles with various Ru/P ratios, *i.e.* Ru<sub>2</sub>P and RuP, exploiting white phosphorus as 'P'-source. A thorough characterization of these nanoparticles revealed that their actual structure and their chemical state was very different compared to other TMPs (Transition Metal Phosphides) NPs previously reported. Afterwards, a colloidal dispersion of the synthesized Ru–P nanostructures was tested in the hydrogenation of substituted nitroarenes to the corresponding aromatic primary amines.

## Results and Discussion

### Synthesis and characterization of nanostructured Ru-P nanoparticles

The original Mézailles<sup>[22]</sup> two-step protocol to prepare Ni<sub>2</sub>P nanoparticles consisted first in the preparation of Ni(0) NPs by thermal decomposition of Ni(acac)<sub>2</sub> at 220 °C in the presence of oleylamine as reductant and TOP (*tris-n-octylphosphine*) as stabilizing agent, followed by treatment with P<sub>4</sub>.<sup>[18]</sup>

However, using Ru(acac)<sub>3</sub> as precursor under similar conditions, either in the presence or absence of TOP as ligand, this protocol turned out unsuccessful to prepare Ru(0) NPs. Thus, the method reported by Can and Metin was followed.<sup>[23]</sup> More specifically, a mixture of Ru(acac)<sub>3</sub>, oleylamine and dibenzylether was degassed at 110 °C, then quickly brought to 300 °C and kept at this temperature for one hour.

XRD measurements of the material recovered after workup confirmed the successful growth of metallic Ru(0) NPs. The powder spectrum only featured one broad peak at 2θ° = 42° (FWHM ≈ 6°), alongside a weak bump at high angle centered around 2θ° = 84°, see Figure 1. The main peak was assigned to the (011) reflection of hexagonal Ru, overlapping with the (002) and (010) reflections, severely broadened by the nanometric size of the crystallites and eventually by their imperfect crystallinity. The bump at 2θ° = 84° also matches the weaker high angle reflections of the Ru reference. Binary ruthenium-phosphorus nanoparticles with different Ru:P ratio were obtained by addition of the appropriate amount of P<sub>4</sub> to a suspension of Ru(0) NPs in oleylamine (Scheme 1). In the first attempts, the exact stoichiometric amount of white phosphorus was used for the synthesis of Ru<sub>2</sub>P and RuP. However, ICP-AES analysis of the isolated nanoparticles revealed the nanocompo-

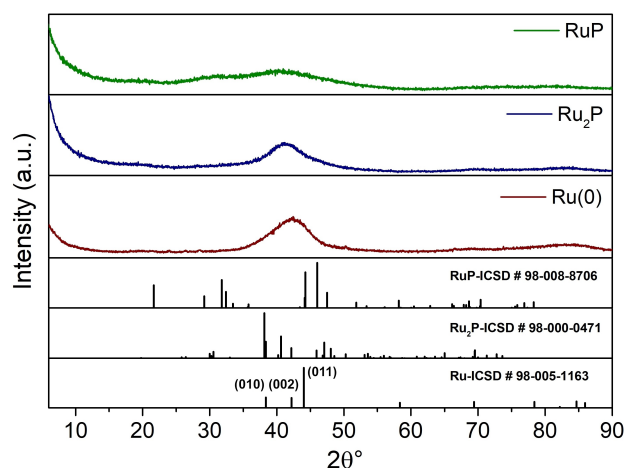
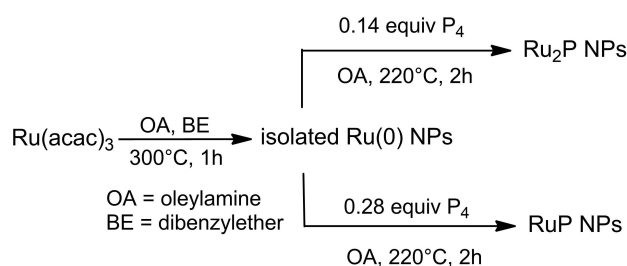


Figure 1. Powder XRD spectra of Ru(0), Ru<sub>2</sub>P and RuP NPs.



Scheme 1. Preparation of Ru–P nanoparticles by a two-step procedure.

sites to be in defect of phosphorus, which was subsequently accounted for by adding a slight excess of P<sub>4</sub> (Scheme 1) to obtain the desired stoichiometry of each Ru-phosphide.

The Ru–P NPs were then isolated by repeated centrifugation and washing steps. Notably, ICP measurements confirmed the expected chemical composition of the two Ru–P NPs, with Ru:P ratio equal to 1.97 (±0.16) for Ru<sub>2</sub>P and equal to 1.08 (±0.03) for RuP, see Table S1. The content of capping oleylamine was quantified in *ca.* 44 wt.% and 32 wt.% for Ru<sub>2</sub>P and RuP, respectively. The XRD pattern of Ru<sub>2</sub>P (see Figure 1) closely resembles the one of Ru(0) NPs, except for the nearly disappearance of the weak bump around 2θ° = 84°, suggesting that the uptake of phosphorus had minor effect on the overall lattice structure. Interestingly, increasing the amount of phosphorus up to a 1:1 ratio led to the collapse of the main peak at 2θ° = 42°, leaving the XRD spectrum of RuP almost featureless, which strongly points to an amorphization of the nanoparticles.

The morphology of the Ru–P NPs was ascertained by bright field TEM (transmission electron microscopy) using colloidal dispersions drop-casted on a carbon/copper grid. As shown in Figures 2b and 2c, the nanoparticles were homogeneous in both shape and dimension. The relative size distribution histogram (measured on roughly 70 particles) showed an average diameter  $d = 3.3 \pm 0.7$  nm in the case of Ru<sub>2</sub>P NPs (Figure 2b) and  $d = 3.4 \pm 0.6$  nm for RuP NPs (Figure 2c), which is slightly

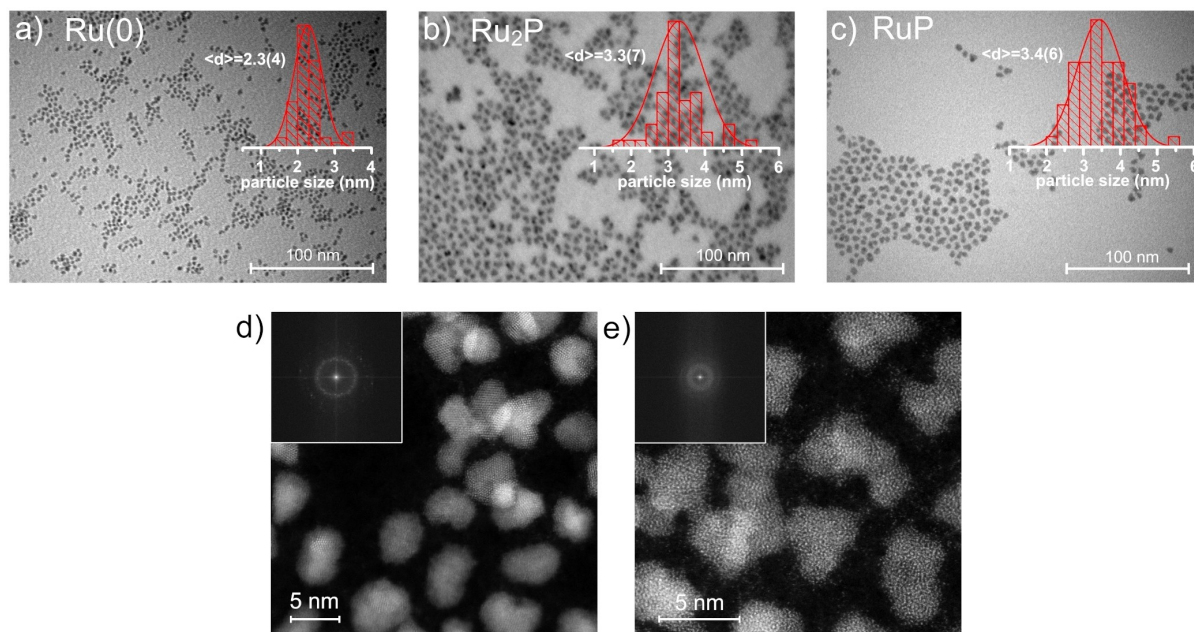


**Figure 2.** Bright field TEM image of (a) Ru(0), (b) Ru<sub>2</sub>P NPs and (c) RuP NPs, with relative size distribution histogram. HAADF-STEM with inset of FFT pattern of (d) Ru<sub>2</sub>P NPs and (e) RuP NPs.

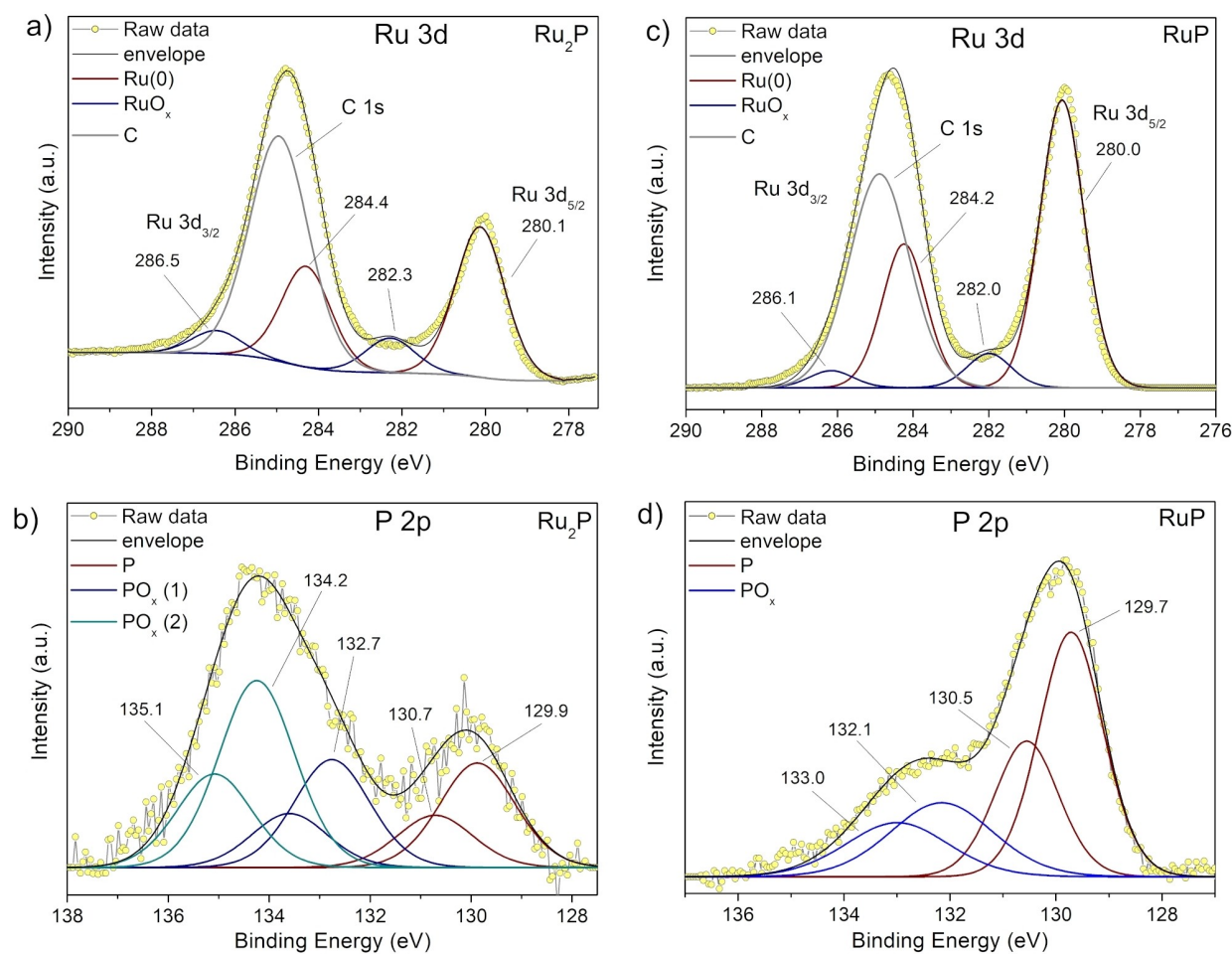


**Figure 3.** XPS spectra of Ru<sub>2</sub>P and RuP NPs at the C1s and Ru 3d core levels (a, b) and the P 2p core level (c,d).

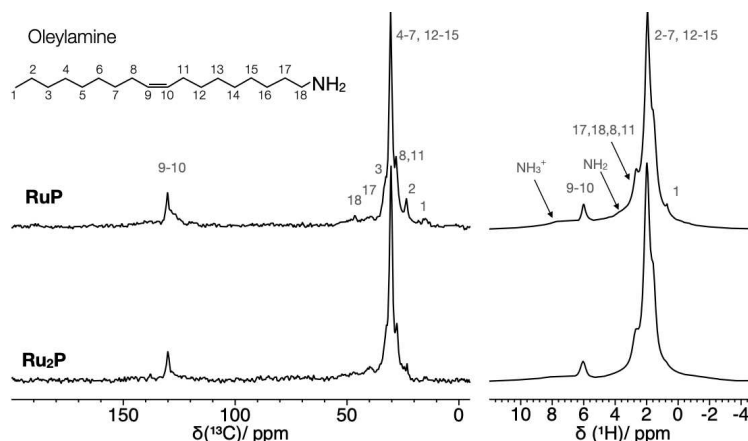


**Figure 4.**  $^{13}\text{C}$  CP MAS (left) and  $^1\text{H}$  MAS (right) spectra, recorded at a MAS frequency of 20 kHz, of RuP and  $\text{Ru}_2\text{P}$  with signals assignment. In the inset the chemical formula of oleylamine is reported with numbering of the atoms (same number is used for bonded  $^1\text{H}$  and  $^{13}\text{C}$  atoms).

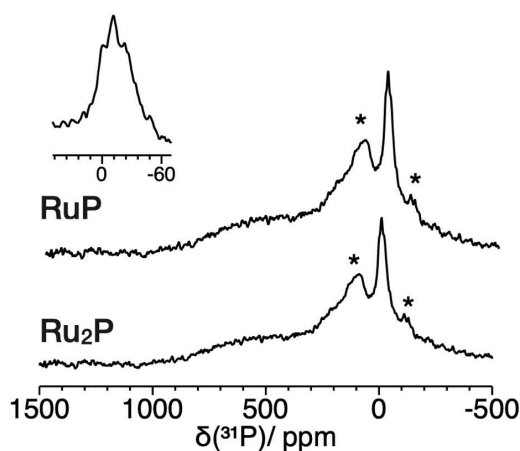


**Figure 5.**  $^{31}\text{P}$  MAS spectra of RuP (top) and  $\text{Ru}_2\text{P}$  (bottom). Spectra have been recorded using Hahn echo (HE) sequence. Spinning sidebands are marked with asterisks. The spectral region at low chemical shifts is expanded in the inset of the figure.

larger than the precursor Ru(0) NPs, having average size  $d = 2.3 \pm 0.4$  nm, see Figure 2a.

To shed light on the different behavior observed under X-Ray diffraction and gain an insight on the structure at lattice resolution, HAADF-S/TEM (high angle annular dark-field scanning transmission electron microscopy) imaging was carried out on the two stoichiometries. Intriguingly, analyzing a series of nanoparticles from each sample, it turned out that a certain degree of crystallinity is observed in the case of  $\text{Ru}_2\text{P}$ , likely arising from the metallic ruthenium domains originating from the precursor Ru(0) NPs and retained in  $\text{Ru}_2\text{P}$ . The relative lattice fringes are clearly visible in the high resolution micrograph (see Figure 2d) in agreement with XRD shown in Figure 1, where the pattern of Ru(0) and  $\text{Ru}_2\text{P}$  NPs are almost superimposable. On the contrary, an amorphous structure was evidenced for RuP (see Figure 2e). This can be attributed to the larger amount of P atoms which had diffused in the ruthenium lattice in the case of RuP stoichiometry, with loss of the long-range order. From

the Fast Fourier Transform (FFT) pattern of  $\text{Ru}_2\text{P}$ ,  $d_{hkl}$  spacings were obtained, which agreed within  $\pm 0.1$  Å to the values reported for the (010), (002) and (011) crystallographic planes in hexagonal Ru.<sup>[24]</sup> Correspondingly, the FFT pattern of RuP further assessed its amorphous nature. Energy-dispersive X-ray spectroscopy (EDS) carried out on the lattice scale confirmed the chemical identity and purity of the samples, with relative percentage of ruthenium and phosphorus in close agreement with the values found by ICP-AES, see Figure S1, S2 and Table S1.

Inspection of the two samples by EELS (electron energy loss spectroscopy) evidenced an intriguing difference in the phosphorus distribution: in the case of  $\text{Ru}_2\text{P}$  a concentration gradient was observed, with phosphorus being mainly localized in the outer shell of the NPs, while the core appeared richer in ruthenium, as shown in Figure S3. This was also confirmed by running an EDS mapping (see Figure S4). Moving to the phosphorus-rich RuP phase, phosphorus appeared homogeneously distributed within the nanoparticles, as evidenced by EELS mapping in Figure S5. Thus, the diffusion of P atoms to the inner core of the NPs had become important in RuP.

The chemical nature and environment of ruthenium, phosphorus and carbon atoms located at the surface of the nanoparticles were analyzed by high resolution XPS measurements. Figure 3 displays XPS spectra of the C 1s, Ru 3d and the P 2p core levels for both samples  $\text{Ru}_2\text{P}$  and RuP. The very intense peak of C at 284.8 eV, typical of organic carbon, agrees well with the presence of oleylamine on the nanoparticles surface as capping agent. The Ru 3d core transition is characterized by a doublet due to the spin-orbit coupling, namely the  $3d_{5/2}$  and  $3d_{3/2}$  components, though the latter is masked by the overlapping with the carbon C 1s transition. Interestingly, the component responsible for the larger amount of the signal is located at binding energy (B.E.) values typical of Ru in (0)-oxidation state (B.E.  $3d_{5/2} = 280.1 \pm 0.1$  eV), and was attributed to a metallic state of Ru within the nanoparticles.<sup>[25]</sup> The minor and more oxidized component (B.E.  $3d_{5/2} = 282.3 \pm 0.1$  eV) accounts for the presence of some ruthenium oxides, in

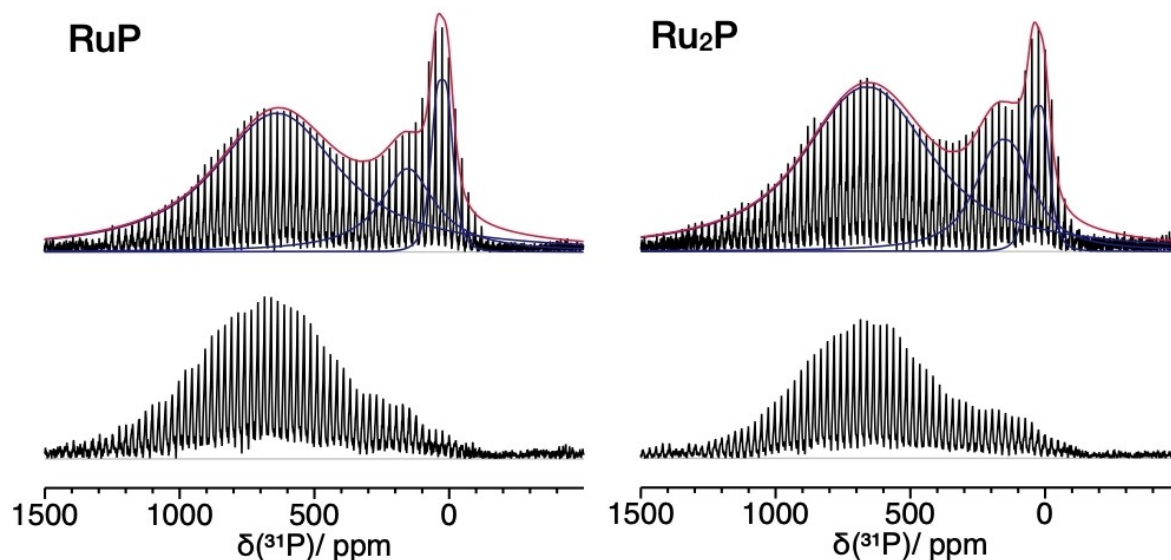


**Figure 6.** Static  $^{31}\text{P}$  WURST-CPMG spectra of RuP and  $\text{Ru}_2\text{P}$ . Spectra were recorded with a recycle delay of 5 s (top) and 0.2 s (bottom). For quantitative spectra (top) the spectral fitting is also reported (single peaks in blue and the sum of the three contributions in red).

+IV or +VI oxidation state, formed on the surface of the nanoparticles,<sup>[26,27]</sup> a feature commonly observed with nanosized ruthenium upon air exposure. No difference was observed in the spectra between the two stoichiometries. The presence of ruthenium in zero oxidation state was accompanied by the observation of a component in the phosphorus P 2p spectrum having P 2p<sub>3/2</sub> B.E. = 129.9 eV and P 2p<sub>1/2</sub> B.E. = 130.7 eV, which is typical of phosphorus in its elemental state.<sup>[28,29]</sup> The other oxidized phosphorus contributions were safely assigned to minor surface PO<sub>x</sub> species in varying amount depending on the sample, arising from air oxidation. The zero-valence of Ru and P points out that no relevant electron density transfer takes place between the two elements, though this would be expected for a metallic phosphide featuring P<sup>δ-</sup> units. In contrast, these nanoparticles are better described as a ruthenium-phosphorus alloy, with negligible polarization and retention of the metallic character of Ru. Notably, the growth of thin-films of amorphous Ru–P alloy by CVD approaches has been described,<sup>[30]</sup> as well as the preparation of a colloidal Ru–P alloy system using H<sub>2</sub>PO<sub>2</sub><sup>-</sup> as P-source.<sup>[31]</sup>

In agreement with the presence of capping oleylamine on the surface of the NPs, the N 1s core level spectrum of sample RuP (see Figure S6) was characterized by a signal at B.E. = 398.9 eV, corresponding to the amine group.<sup>[32]</sup> The additional weaker peak at higher binding energy B.E. = 401.8 eV was assigned to minor protonated oleylamine.

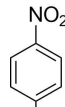
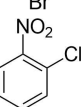
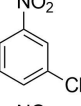
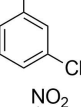
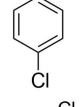
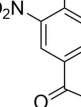
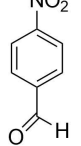
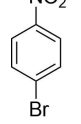
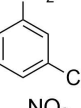
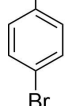
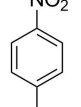
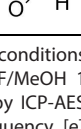
To gain a better understanding of the actual nature of phosphorus and ruthenium in the NPs, complementing the information gained from microscopy and XPS, a detailed multinuclear Solid State NMR (SS NMR) study was carried out.  $^1\text{H}$  and  $^{13}\text{C}$  MAS (Magic Angle Spinning) spectra (Figure 4) allowed the observation of the expected signals of oleylamine. It is interesting to notice that the  $^1\text{H}$  signals of the amine group, both neutral and protonated, show a peculiar broadening, due

to the direct interaction with the surface of the NPs.<sup>[33]</sup> No significant differences are observed between the spectra of RuP and  $\text{Ru}_2\text{P}$ .

As far as phosphorus is concerned, several papers have been published reporting  $^{31}\text{P}$  SS NMR spectra of transition metal phosphides,<sup>[34,35,36,37]</sup> but only a few on Ru phosphides,<sup>[38,39,40]</sup> remarkably, a direct correlation between the  $^{31}\text{P}$  SS NMR response and the electronic structure of some transition metal phosphides<sup>[41,42]</sup> has been demonstrated. However, the systems investigated in the literature are typical stoichiometric crystalline phosphides, while, to the best of our knowledge, an NMR study of ruthenium-phosphorus alloys has not been reported yet.  $^{31}\text{P}$  MAS spectra (Figure 5) show in the low chemical shifts region, three peaks at  $\delta = 0.8$ ,  $-11.0$  and  $-24.3$  ppm, ascribable to phosphate, pyrophosphate and polyphosphate species respectively, arising from phosphorus oxidation, reasonably occurring at the surface of the NPs, as already observed by XPS. At higher frequencies the  $^{31}\text{P}$  MAS spectra show two additional broad peaks, centered at about  $\delta = 90$  and 550 ppm.

By recording  $^{31}\text{P}$  MAS spectra at different values of irradiation frequency it was clear the impossibility of a homogeneous irradiation of the whole spectra in a single step. Thus, we resorted to the WURST-CPMG experiment,<sup>[43,44]</sup> designed for the reliable and time-saving acquisition of ultrawide SS NMR spectra, which allowed us to record sound  $^{31}\text{P}$  spectra of RuP and  $\text{Ru}_2\text{P}$  (Figure 6). To the best of our knowledge this is the first time that WURST-CPMG is applied to  $^{31}\text{P}$ .

The comparison between WURST-CPMG and MAS spectra clearly shows that in the latter the intensity of the broadest peak, resonating at highest frequency, is largely underestimated. The fitting of WURST-CPMG patterns (Figure 6) highlights that the spectra of both samples can be well reproduced with three peaks: one due to oxidized P species centered at  $\delta = 24$  ppm (that is higher than the corresponding isotropic

Table 1. Hydrogenation of functionalized nitroarenes using Ru-based catalyst. <sup>[a]</sup>						
Catalyst	Substrate	Time [h]	Sub/C <sup>[b]</sup>	Conv. <sup>[c]</sup> [%]	Select. <sup>[c]</sup> [%]	TOF <sup>[d]</sup> [h <sup>-1</sup> ]
Ru <sub>2</sub> P		1	152	98.2	98.7	150
		1.5	152	99.3	99.8	101
		1	152	99.4	99.8	152
		1 <sup>[e]</sup>	152	95.8	99.8	146
		1	152	99.2	99.0	152
		1.5	152	99.7	99.0	101
RuP		1.5 <sup>[f]</sup>	152	99.8	89.7	101
		1	206	1.0	99.8	2
		1	206	1.0	99.8	2
		1.5	76	68	98.7	35
Ru(0)		1.5 <sup>[f]</sup>	76	99.9	89.7	50
		1.5 <sup>[f]</sup>	76	99.9	89.7	50

[a] Reaction conditions: 0.29 mmol of substrate, T = 66 °C; P H<sub>2</sub> = 10 bar; V = 2 mL (THF/MeOH 1 : 1); [b] Sub/C = substrate to catalyst molar ratio, determined by ICP-AES. [c] Data from GC analysis and GC-MS; [d] TOF = turn over frequency. [e] Test of ambient stability. [f] p(H<sub>2</sub>) = 5 bar.

chemical shifts observed in the MAS spectra because of the effect of chemical shielding anisotropy under non-MAS conditions), representing 8–10% of P nuclei (percentages refer to RuP and Ru<sub>2</sub>P, respectively), the other two peaks are centered at  $\delta = 152$  ppm and 636 ppm, and represent 21–20% and 71–70% of P nuclei, respectively. The shift at  $\delta = 636$  ppm can be ascribed to a positive Knight shift contribution to the resonance frequency of phosphorus due to the effect of Ru conduction electrons<sup>[37,38]</sup> and agrees with the formation of a Ru–P alloy, with both elements in zero oxidation state, as found by XPS. The high percentage of this kind of P atoms suggests that they are located not only at the surface but also in the bulk of the NPs, as shown above by EELS mapping, see Figures S3 and S5. The Knight shift observed is slightly smaller than that reported for crystalline RuP<sup>[34–36]</sup> and this could be due to a less intimate and homogeneous mixing among the elements. For the <sup>31</sup>P peak observed at 152 ppm, representing about 20% of P atoms, the Knight shift is considerably smaller and this can be ascribed to a lower local concentration of Ru atoms around P nuclei.<sup>[45]</sup> Both peaks at 636 and 152 ppm show a large linewidth, unaffected by MAS, which can result from the very small size of the nanoparticles<sup>[38]</sup> and from a distribution of shifts due to different environments of the P nuclei, consistently with the lack of a definite phosphide lattice as revealed by HAADF-STEM and XRD results. The electronic effect exerted by ruthenium atoms on P nuclei at 636 and 152 ppm is also confirmed by their fast spin-lattice relaxation, evident from the comparison between spectra recorded by using two different recycle delays (Figure 6): the intensity of the signals at 636 and 152 ppm has fully and mainly recovered its maximum value when a recycle delay of 0.2 s is used (differently from the signal of phosphates that requires a recycle delay of 5 s).

### Catalytic Selective Hydrogenation of Nitroarenes

Ruthenium phosphide phases have recently gained growing interest as innovative cathode materials for the hydrogen evolution reaction (HER), with particular attention devoted to the understanding of structure<sup>[46]</sup> and support effects.<sup>[47]</sup> To date little has been explored of Ru–P reactivity aside from electrocatalytic applications and as far as we know there is no report of the application of Ru–P NPs in the reduction of nitroarenes. This prompted us to test the catalytic activity of the prepared Ru–P nanoalloys in the reduction of a series of industrially relevant nitroarenes<sup>[48]</sup> to the corresponding anilines. Using very mild conditions, that is T = 66 °C and hydrogen gas as reducing agent at 10 bar of pressure avoiding the use of highly toxic NaBH<sub>4</sub> or N<sub>2</sub>H<sub>4</sub>, chloro- and bromo-nitroarenes were successfully converted to the desired haloaniline with high activity and excellent chemoselectivity without observing any dehalogenation, see Table 1.

The reaction products were quantified by GC and identified by GC-MS and <sup>1</sup>H NMR as shown in the Supporting Info, see Figures S7–S16. The trend in the catalytic activity follows the order Ru<sub>2</sub>P > Ru > RuP NPs with a four-fold increase of the TOF on going from Ru(0) NPs to Ru<sub>2</sub>P NPs which can be related to a

**Table 2.** Comparison of nanostructured Ru-based catalyst in the reduction of nitroarenes.<sup>[a]</sup>

Entry	Catalyst	Substrate	Time [h]	T [°C]	Reducing agent	Conv. [%]	Select. [%]	Ref.
1	Ru <sub>2</sub> P	<i>p</i> -CNB	1	66	H <sub>2</sub> <sup>[b]</sup>	99.2	99.0	this work
2	RuNPs	<i>m</i> -BNB	1.5	100	NaBH <sub>4</sub>	100	89 <sup>[d]</sup>	45
3	Ru/rGO	<i>p</i> -CNB	2	60	H <sub>2</sub> <sup>[c]</sup>	100	96	46
4	Ru/SBA	nitroarene	21	80	N <sub>2</sub> H <sub>4</sub>	100	> 99	47
5	Ru/UiO-66	<i>p</i> -CNB	5	150	HCOOH	100	> 99	48
6	Ru/C	<i>p</i> -BNB	12	120	EtOH	100	92	49

[a] *p*-CNB: *para*-chloronitrobenzene; *m*-BNB: *meta*-bromonitrobenzene; *p*-BNB: *para*-bromonitrobenzene; [b] 10 bar; [c] 30 bar; [d] isolated. Since table 2 is a collection of different lit. data, where conv% may be evaluated in different manner, it is convenient to remove the headings from conv% and select%.

synergistic cooperation between Ru and P in the activation of molecular hydrogen<sup>[12]</sup> at the surface of the NPs. Doing a survey of the literature,<sup>[49,50,51,52]</sup> much more drastic conditions (longer reaction time, higher temperature, excess of reducing agent) are necessary, as shown in Table 2, once the reaction is carried out in the presence of nanostructured Ru(0)-based catalyst either in a colloidal form (entry 2) or supported (entry 3–6), revealing the powerful role of P-alloying.

The dramatic drop of the reaction rate observed in the presence of RuP, can be accounted for by the different chemical composition and structure of the nanoparticles surface as compared with Ru<sub>2</sub>P. The higher percentage of P atoms on the surface of RuP as highlighted by EELS analysis shown in Figure S5, strongly contributes to dilute the active metal-metal ensembles necessary for hydrogenation<sup>[53]</sup> and thus hamper the absorption of the reactants, hydrogen and nitroarene. Indeed, even for *classical* phosphides, the metal-rich Ru<sub>2</sub>P is known to be a more active phase than RuP and metal Ru for several catalytic processes.<sup>[1,12,44]</sup> Noteworthy, a very high selectivity was observed in particular in the reduction of chloro- and bromonitrobenzene, for which it is quite common the formation of by-products deriving from the hydrogenolysis of the carbon-halogen bond. 54 Recycling tests were performed for the hydrogenation of *meta*-chloronitrobenzene using Ru<sub>2</sub>P, and the selectivity was preserved, while a slight decrease of the conversion was observed, see Table S2, correlated to an observed diminution of the catalyst suspendability. 55 TEM-EDS measurements were carried out on the catalyst recovered after recycling tests, and confirmed that Ru<sub>2</sub>P NPs maintained their initial size ( $d=3.6(3)$  nm) and their elemental composition, see Figures S17 and S18 respectively, though a certain aggregation was observed. Additionally, to verify the ambient stability, a suspension of Ru<sub>2</sub>P was left exposed to air for twenty days before running a catalytic test and showed the same conversion and selectivity as a fresh sample, see Table 1.

## Conclusions

A reproducible and scalable method for the synthesis of Ru–P nanoalloy has been developed based on the use of white phosphorus as P-source and encompassing mild reaction conditions, which allows a precise control of the stoichiometry of the binary derivatives Ru<sub>2</sub>P and RuP, and of the size

distribution (average 3.3 nm) and morphology of the nanoparticles. This protocol outperforms the known synthetic procedures based on high-temperature treatment that affords larger particles (4–20 nm), often featuring aggregates and polydispersity. A comprehensive investigation of the nanoparticles structure and the chemical state of Ru and P was carried out by means of HAADF-STEM, XRD, and XPS respectively. The latter revealed that both elements are present in *zero*-oxidation state. EELS mapping evidenced that the radial distribution of P atoms in the two Ru–P systems is different hinting for a different chemical reactivity at the surface. For the first time, the <sup>31</sup>P nuclei within nanostructured Ru–P systems were probed using the WURST-CPMG NMR pulse sequence. The NMR spectra highlighted that most P nuclei are in close vicinity of Ru atoms and participate to their electron conduction band. The catalytic activity of Ru–P NPs was evaluated in the selective hydrogenation of substituted nitroarenes to the corresponding primary amines and evidenced how the incorporation of P atoms can finely tune the surface properties and P-dosage is a critical parameter. Indeed, while Ru<sub>2</sub>P showed a four-fold improvement in the catalytic activity compared with Ru NPs giving very high chemoselectivity (> 99%) at complete conversion, RuP ended up with sluggish activity. Further studies are in progress to explore the application of these nanostructured Ru–P alloys in different catalytic processes.

## Experimental section

### Materials

All reactions were carried out under nitrogen atmosphere. All the solvents used were of analytical grade except for oleylamine, which was of technical grade (Aldrich, 70%) and was used as received. Methanol and THF were purified by distillation over CaH<sub>2</sub> and Na/benzophenone, respectively. They were degassed prior to use. Ru(acac)<sub>3</sub> was prepared according to literature.<sup>[56]</sup> White phosphorus was taken from the laboratory's own chemical stockroom, where it was regularly stored under water.

### Synthesis of Ru–P nanoparticles

The synthesis of Ru–P nanoparticles was carried out by a two steps procedure, which implied the isolation of the initially formed Ru(0) NPs followed by their resuspension in fresh solvent and reaction with P<sub>4</sub>.



### STEP a) Synthesis of Ru NPs

The preparation of Ru NPs was carried out following the procedure by Can and Metin,<sup>[23]</sup> with minor modifications. A suspension of Ru(acac)<sub>3</sub> (399.0 mg, 1.0 mmol) in technical oleylamine (20 mL) and dibenzylether (16 mL) was degassed with three vacuum/N<sub>2</sub> cycles at 110 °C inside a Schlenk flask. The suspension was then heated up to 300 °C and kept at this temperature for one hour. After this time the resulting black dispersion was cooled down to RT. Degassed 2-propanol (40 mL) was added and after centrifugation at 10000 rpm the nanoparticles were isolated and dried under a nitrogen stream. The yield of this first step was established in a separate experiment to be 90% by ICP-AES analysis. The Ru content amounted to ca. 55 wt.%, the remaining 45 wt.% consisting in capping oleylamine.

### STEP b) Synthesis of Ru<sub>2</sub>P NPs

The Ru NPs prepared as described in STEP a), corresponding to 91 mg of Ru content (0.90 mmol) were dispersed in degassed oleylamine (20 mL) and transferred in a Schlenk flask. A solution of P<sub>4</sub> in toluene was added (0.82 mL, 0.15 M in P<sub>4</sub>, 0.55 eq of 'P') and toluene was removed under vacuum at room temperature. A slight excess of P<sub>4</sub> is needed to compensate for minor losses during toluene removal. The suspension was quickly heated up to 220 °C and kept at this temperature for 2 hours. After this time the dispersion was cooled down to RT. 40 mL of degassed 2-propanol were added and after centrifugation at 10000 rpm for 30 minutes, the nanoparticles were isolated. Three additional washing cycles were repeated upon resuspension of the NPs in toluene (10 mL of toluene followed by 40 mL of 2-propanol). The same procedure was followed to prepare **RuP NPs**, using 1.1 eq 'P' (1.64 mL, 0.15 M in P<sub>4</sub>). The stoichiometry of the prepared nanoparticles as determined by ICP-AES was very close to the expected integer values (*i.e.* RuP and Ru<sub>2</sub>P, see Table S1). The same results were obtained repeating the synthesis on a smaller scale (*i.e.* from 40 or 100 mg of Ru(acac)<sub>3</sub>). Stock solutions to be used in catalysis were prepared suspending the nanoparticles in distilled THF.

### Catalytic hydrogenation

In a typical run, Ru<sub>2</sub>P (or RuP or Ru) NPs in THF (1.00 mL, 0.0019 M in [Ru], 0.0019 mmol) were added in a glass vial, followed by 1.0 mL of degassed MeOH. The nitroarene substrate was added and the mixture was sonicated to dissolve the substrate and better disperse the NPs. The glass vial was placed inside a 50 mL autoclave equipped with a PTFE lining and was purged with hydrogen (x 5) and then pressurized up to 10 bar. The mixture was kept stirring at 66 °C for the required time, after which the gas was vented and the autoclave was cooled to room temperature. The resulting mixture was transferred in a centrifuge tube, 2 mL of degassed MeOH were added and the suspension was centrifuged at 9000 RPM for 30 minutes. The supernatant was collected and analyzed by GC and GC-MS.

### GC and GC-MS analysis of the reaction products

After each reaction had stopped, the autoclave was put in an ice bath and cooled down. Then, it was depressurized and opened, 100 µL of the reaction mixture were taken and filtered over alumina. The filtrate was analyzed by GC using a Shimadzu GC-2010 instrument equipped with a flame ionization detector (FID) and a polar capillary column VF-WAXms (30 m, 0.25 mm i.d., 0.25 µm film thickness). The products were identified by GC-MS using GCMS-QP2010 Shimadzu instruments equipped with a column identical to that previously described.

### <sup>1</sup>H NMR analysis of the reaction products

<sup>1</sup>H NMR was recorded on a Bruker Avance II 400 spectrometer (operating at 400.13 MHz) and peak positions are relative to tetramethylsilane.

### Elemental Analysis

Samples of the prepared ruthenium phosphide nanoparticles were analyzed by Inductive Coupled Plasma-Atomic Emission Spectroscopy (ICP-AES) in order to determine the exact stoichiometry and the metal content in the dry powder. Samples followed a digestion in aqua regia (HNO<sub>3</sub> : HCl in molar ratio 3:1) over 7 days, during which time they were regularly treated with ultrasounds (10 minutes each day). The prolonged digestion was due to the reluctancy of the nanoparticles capped with hydrophobic oleylamine to be wetted and dissolved by the acidic solution. In particular, a complete digestion was mandatory to calculate reliable concentrations for the stock solutions used in catalysis. Measurements were performed with an Agilent 7700 Series spectrometer at the Chemistry Department, University of Florence (Italy). From ICP-AES analysis the content of ruthenium metal resulted 48% and 52% in weight for Ru<sub>2</sub>P and RuP, respectively.

### Powder X-ray diffraction

Powder XRD measurements were performed using an X'Pert PRO diffractometer operating in reflection mode with CuKα radiation with 40 kV beam voltage and 40 mA current. The data were collected in the 5°–90° 2θ range, with steps of 0.01° and counting time of 130 s.

### Transmission electron microscopy (TEM)

TEM studies of the nanoparticles were carried out using a Philips instrument operating at an accelerating voltage of 80 kV. Samples were prepared by air-drying few drops of a tetrahydrofuran suspension of the nanoparticles on a TEM copper/carbon grid.

**HAADF-S/TEM (High-Angle Annular Dark Field Scanning Transmission Electron Microscopy).** Atomic-resolution characterization by S/TEM was performed through a probe aberration-corrected JEOL ARM200CF, equipped with a Ceos hexapole-type Cs corrector, named CESCOR, and operated at a primary beam energy of 200 keV. The electron gun is a cold-field emission gun with an energy spread of 0.3 eV. The probe size was 0.65 Å at 200 kV. Micrographs were acquired in Z-contrast mode.

**EDS.** A Centurio Energy Dispersive Spectrometer (EDS) equipped with a 100 mm<sup>2</sup> Silicon Drift Detector was used for the EDS acquisitions.

**EELS.** A GIF Quantum ER as Electron Energy Loss Spectrometer (EELS) was used for EELS measurements. Both low- and core-loss EELS spectra were acquired with the DualEELS capability through Gatan Digital Micrograph software, which allows the accurate energy calibration of EELS spectra, thanks to the simultaneous alignment of the zero-loss peak position for every single acquisition, which removes any artefact coming from energy shifts. The use of Fourier logarithmic deconvolution on a full spectrum obtained by splicing together low- and core-loss EELS allows removing thickness-related plural scattering.<sup>[57]</sup> All the STEM-EELS and STEM-EDS measurements were performed simultaneously by using the Gatan spectrum imaging (SI) tool.

## X-ray Photoelectron Spectroscopy (XPS)

XPS measurements were performed in an ultra-high vacuum (10–9 mbar) system equipped with a VSW HAC 5000 hemispherical electron energy analyzer and a non-monochromatized Mg-K $\alpha$  X-ray source (1253.6 eV). The source power was 100 W (10 kV  $\times$  10 mA) and the spectra were acquired in the constant-pass-energy mode at Epas = 44 eV. The overall energy resolution was 1.2 eV as a full-width at half maximum (FWHM) for the Ag 3d5/2 line of a pure silver reference. The recorded spectra were fitted using XPS Peak 4.1 software employing Gauss-Lorentz curves after subtraction of a Shirley-type background. The powder sample was introduced in the UHV system via a loadlock under inert gas (N<sub>2</sub>) flux, in order to minimize the exposure to air contaminants and kept in the introduction chamber for at least 12 hours before the measurements.

## Solid State NMR Spectroscopy

Solid State NMR (SS NMR) spectra were recorded on a Bruker Avance Neo spectrometer working at Larmor frequencies of <sup>1</sup>H, <sup>13</sup>C and <sup>31</sup>P nuclei of 500.13, 125.77, 202.46 MHz, respectively, using a double-resonance fast Magic Angle Spinning (MAS) probehead accommodating rotors with an external diameter of 1.3 mm.

<sup>31</sup>P MAS spectra were recorded using a Hahn Eco (HE) pulse sequence under SPINAL decoupling from <sup>1</sup>H nuclei. <sup>31</sup>P spectra were also acquired with Wideband Uniform Rate Smooth Truncation – Carr–Purcell Meiboom–Gill (WURST-CPMG)<sup>[43,44]</sup> pulse sequence in static conditions. 100  $\mu$ s pulse width and WURST-100000 pulse shape were used for WURST-CPMG experiments, with a nutation frequency of 95 kHz. 158 Maiboom–Gill loops were acquired with an echo duration of 80  $\mu$ s, and sweep range of 1 MHz. Recycle delays of 5 s and 0.2 s were used accumulating between 8000 and 16000 transients.

The <sup>31</sup>P chemical shift scale was referred to the signal of H<sub>3</sub>PO<sub>4</sub> 80% at 0 ppm.

<sup>13</sup>C MAS spectra were recorded using (<sup>1</sup>H-<sup>13</sup>C) Cross Polarization, with a contact time of 2 ms, under SPINAL decoupling from <sup>1</sup>H nuclei. 10000 transients were accumulated with recycle delay of 1 s. The <sup>1</sup>H MAS spectra were recorded at a MAS frequency of 20 kHz, accumulating 40 transients with a recycle delay of 1 s. All spectra were recorded at 298 K.

## Supporting Information

The Supporting Information contains supplementary Tables, EDS, EELS, XPS and TEM figures, GC-MS and <sup>1</sup>H NMR spectra and it is available free of charge.

## Acknowledgements

We thank the European Union (Marie Curie ITN SusPhos, Grant Agreement No. 317404) for financial support. SusPhos financed the stay of F. Delgado Calvo in the group of N. Mézailles at CNRS in Toulouse. CISUP (Centre for Instrument Sharing-University of Pisa) is acknowledged for the use of the Bruker Avance NEO 500 Solid State NMR spectrometer. Part of this work has received funding from the European Union's Horizon 2020 research and innovation programme under grant agreement No 823717 – ESTEEM3. The authors gratefully acknowledge “Ce.M.E.-Centro

Microscopie Elettroniche Laura Bonzi” in Sesto Fiorentino, Italy and Dr. Cristina Salvatici for running TEM-EDS measurements. Open Access funding provided by Consiglio Nazionale delle Ricerche within the CRUI-CARE Agreement.

## Conflict of Interest

The authors declare no conflict of interest.

## Data Availability Statement

The data that support the findings of this study are available from the corresponding author upon reasonable request.

- [1] R. H. Bowker, M. C. Smith, M. L. Pease, K. M. Slenkamp, L. Kovarik, M. E. Bussell, *ACS Catal.* **2011**, *1*, 917–922.
- [2] Y. Kanda, C. Temma, K. Nakata, T. Kobayashi, M. Sugioka, Y. Uemichi, *Appl. Catal. A: General* **2010**, *386*, 171–178.
- [3] R. H. Bowker, M. C. Smith, B. A. Carrillo, M. E. Bussell, *Top. Catal.* **2012**, *55*, 999–1009.
- [4] Q. Guan, C. Sun, R. Li, W. Li, *Catal. Commun.* **2011**, *14*, 114–117.
- [5] H. Zhang, A. W. Majenburg, X. Li, S. L. Schweizer, R. B. Wehrspohn, *Adv. Funct. Mater.* **2020**, *30*, 2003261.
- [6] J. Yu, Y. Guo, S. She, S. Miao, N. Meng, W. Zhou, M. Liu, Z. Shao, *Adv. Mater.* **2018**, *30*, 1800047.
- [7] Z. Pu, I. Amiinu, W. Li, Z. Kou, S. Mu, *Angew. Chem. Int. Ed.* **2017**, *56*, 11559.
- [8] Q. Chang, J. Ma, Y. Zhu, L. Zhen, D. Xu, X. Duan, W. Peng, Y. Li, G. Zhang, F. Zhang, X. Fan, *ACS Sustainable Chem. Eng.* **2018**, *6*, 6388–6394.
- [9] J. S. Li, J. Y. Li, M. J. Huang, L. X. Kong, Z. Wu, *Carbon* **2020**, *161*, 44–50.
- [10] D. Chen, R. Yu, R. Lu, Z. Pu, P. Wang, J. Zhu, P. Ji, D. Wu, J. Wu, Y. Zhao, Z. Kou, J. Yu, S. Mu, *InfoMat* **2022**, e12287.
- [11] R. Gao, L. Pan, H. Wang, X. Zhang, L. Wang, J.-J. Zou, *ACS Catal.* **2018**, *8*, 8420–8429.
- [12] H. Ishikawa, S. Yamaguchi, A. Nakata, K. Nakajima, S. Yamazoe, J. Yamasaki, T. Mizugaki, T. Mitsudome, *J. Am. Chem. Soc.* **2022**, *2*, 419–427.
- [13] D. Formenti, F. Ferretti, F. K. Scharnagl, M. Beller, *Chem. Rev.* **2019**, *119*, 2611–2680 and references therein.
- [14] J. Gopalakrishnan, S. Pandey, K. K. Rangan, *Chem. Mater.* **1997**, *9*, 2113–2116.
- [15] H. Teller, O. Krichevski, M. Gur, A. Gedanken, A. Schechter, *ACS Catal.* **2015**, *5*, 4260–4267.
- [16] Q. Wang, Z. Wang, X. Yin, L. Zhou, M. A. Zhang, *Mater. Res. Bull.* **2016**, *74*, 98–102.
- [17] J. Liu, M. Meyns, T. Zhang, J. Arbiol, A. Cabot, A. Shavel, *Chem. Mater.* **2018**, *30*, 1799–1807.
- [18] S. Carenco, I. Resa, X. Le Goff, P. Le Floch, N. Mézailles, *Chem. Commun.* **2008**, 2568–2570.
- [19] S. Carenco, Y. Hu, I. Florea, O. Ersen, C. Boissière, N. Mézailles, C. Sanchez, *Chem. Mater.* **2012**, *24*, 4134–4145.
- [20] S. Carenco, M. Demange, J. Shi, C. Boissière, C. Sanchez, P. Le Floch, N. Mézailles, *Chem. Commun.* **2010**, 46, 5578–5580.
- [21] S. Carenco, I. Florea, O. Ersen, C. Boissière, N. Mézailles, C. Sanchez, *New J. Chem.* **2013**, *37*, 1231–1237.
- [22] S. Carenco, C. Boissière, L. Nicole, C. Sanchez, P. Le Floch, N. Mézailles, *Chem. Mater.* **2010**, *22*, 1340–1349.
- [23] H. Can, - Metin, *Appl. Catal. B* **2012**, *125*, 304–310.
- [24] E. O. Hall, J. Crangle, *Acta Crystallogr.* **1957**, *10*, 240–241.
- [25] J. F. Moulder, W. F. Stickle, P. E. Sobol, K. D. J. Bomben, Chastain (Ed.), *Handbook of X-ray Photoelectron Spectroscopy*, Perkin-Elmer Corporation, Minnesota, **1992**.
- [26] D. Rochefort, P. Dabo, D. Guay, P. M. A. Sherwood, *Electrochim. Acta* **2003**, *48*, 4245–4252.
- [27] A. Brandi, S. Caporali, S. Cicchi, L. Lascialfari, M. Muniz-Miranda, S. Orazzini, M. Severi, F. L. Deepak, E. Giorgetti, *Proceedings of the 15th IEEE International Conference on Nanotechnology*, pp. 992–995, **2015**.

- [28] M. Hart, E. R. White, J. Chen, C. M. McGilvery, C. J. Pickard, A. Michaelidis, A. Sella, M. S. P. Schaffer, C. G. Salzmann, *Angew. Chem. Int. Ed.* **2017**, *56*, 8144–8148; *Angew. Chem.* **2017**, *129*, 8256–8260.
- [29] M. Caporali, M. Serrano-Ruiz, F. Telesio, S. Heun, A. Verdini, A. Cossaro, M. Dalmiglio, A. Goldoni, M. Peruzzini, *Nanotechnology* **2020**, *31*, 275708.
- [30] J. Shin, A. Waheed, K. Agapiou, W. A. Winkenwerder, H. W. Kim, R. A. Jones, G. S. Hwang, J. G. Ekerdt, *J. Am. Chem. Soc.* **2006**, *128*, 16510–16511.
- [31] H. Li, D. Chu, J. Liu, M. Quiao, W. Dai, H. Li, *Adv. Synth. Catal.* **2008**, *350*, 829–836.
- [32] D. Wilson, M. A. Langell, *Appl. Surf. Sci.* **2014**, *303*, 6–13.
- [33] D. W. Houck, B. A. Korgel, *Chem. Mater.* **2018**, *30*, 8359–8367.
- [34] T. Bartsch, C. Benndorf, H. Eckert, M. Eul, R. Pöttgen, *Naturforsch.* **2016**, *7*, 149.
- [35] S. T. Oyama, P. Clark, X. Wang, T. Shido, Y. Iwasawa, S. Hayashi, J. M. Ramallo-Lo'pez, F. G. Requejo, *J. Phys. Chem. B* **2002**, *106*, 1913.
- [36] D. Lathrop, D. Franke, R. Maxwell, T. Tepe, R. Flesher, Z. Zhang, H. Eckert, *Solid State Nucl. Magn. Reson.* **1992**, *1*, 73–83.
- [37] I. Furo, I. Bakonyi, K. Tompa, E. Zsoldos, I. Heinmaa, M. Alla, E. Lippmaa, *J. Phys. Condens. Matter* **1990**, *2*, 4217.
- [38] S. Li, Y. Kobayashi, M. Itoh, D. Hirai, H. Takagi, *Phys. Rev. B* **2017**, *95*, 155137.
- [39] G. Z. Fan, R. Y. Chen, N. L. Wang, J. L. Luo, *Chin. Phys. Lett.* **2015**, *32*, 077203.
- [40] E. D. Jones, *Phys. Rev.* **1967**, *158*, 295.
- [41] E. Bekaert, J. Bernardi, S. Boyanov, L. Monconduit, M. L. Doublet, M. Ménétrier, *J. Phys. Chem.* **2008**, *112*, 20481–20490.
- [42] W. Papawassiliou, J. P. Carvalho, N. Panopoulos, Y. Al Wahedi, V. K. S. Wadi, X. Lu, et al. *Nat. Commun.* **2021**, *12*, 4334.
- [43] L. A. O'Dell, R. W. Schurko, *Chem. Phys. Lett.* **2008**, *464*, 97–102.
- [44] A. W. MacGregor, L. A. O'Dell, R. W. Schurko, *J. Magn. Reson.* **2011**, *208*, 103–113.
- [45] L. E. Marbella, J. E. Millstone, *Chem. Mater.* **2015**, *27*, 2721–2739.
- [46] T. Liu, J. Wang, C. Zhong, S. Lu, W. Yang, J. Liu, W. Hu, C. M. Li, *Chem. Eur. J.* **2019**, *25*, 7826–7830.
- [47] Y. Li, Y. Bu, Y. Tao, X. Zhou, H. Yu, J. Yu, L. Tang, Y. Quing, *Chem. Commun.* **2019**, *55*, 7828–7831.
- [48] P. Singh, M. Halder, S. Ray, B. Bandyopadhyay, K. Sen, *ACS Omega* **2019**, *4*, 21267–21278 and references therein.
- [49] G. Y. Fan, W. J. Huang, *Chin. Chem. Lett.* **2014**, *25*, 359–363.
- [50] A. I. Carrillo, K. G. Stamplecoskie, M. L. Marin, J. C. Scaiano, *Catal. Sci. Technol.* **2014**, *4*, 1989–1996.
- [51] Q. Yang, H.-Y. Zhang, L. Wang, Y. Zhang, J. Zhao, *ACS Omega* **2018**, *3*, 4199–4212.
- [52] J. H. Kim, J. H. Park, Y. K. Chung, K. H. Park, *Adv. Synth. Catal.* **2012**, *354*, 2412–2418.
- [53] S. Furukawa, Y. Matsunami, I. Hamada, Y. Hashimoto, Y. Sato, T. Komatsu, *ACS Catal.* **2018**, *8*, 8177–8181.
- [54] F. Costantino, M. Nocchetti, M. Bastianini, A. Lavacchi, M. Caporali, F. Liguori, *ACS Appl. Nano Mater.* **2018**, *1*, 1750–1757.
- [55] It should be pointed out that the catalytic tests were run in THF:MeOH (1:1), because MeOH has a beneficial role in the process (in THF the rate was sluggish), but Ru<sub>2</sub>P NPs are not dispersible in MeOH and in the recycling tests this contributes to the aggregation of the particles.
- [56] T. S. Knowles, M. E. Howells, B. J. Howlin, G. W. Smith, C. A. Amodio, *Polyhedron* **1994**, *13*, 2197–2203.
- [57] J. Scott, P. J. Thomas, M. MacKenzie, S. McFadzean, J. Wilbrink, A. J. Craven, W. A. P. Nicholson, *Ultramicroscopy* **2008**, *108*, 1586.

---

Manuscript received: May 27, 2022  
Revised manuscript received: June 17, 2022  
Accepted manuscript online: June 17, 2022  
Version of record online: July 13, 2022